Supplementary file

Molecular insights into interfacial behavior of crude oil-brine-quartz systems under brine dilution

Zhilin Cheng[1,*], Minrong Xiao[1], Shaokai Tong[2], Shuang Zhang[3], Yuxin Miao[1], Meng Xiao[1]

[1] *School of Petroleum Engineering, Xi'an Shiyou University, Xi'an 710065 , P. R. China*

[2] *Changqing Downhole Technology Company, CNPC Chuanqing Drilling Engineering Company, Xi'an 710021, P. R. China*

[3] *Research Institute of Exploration & Development, PetroChina Liaohe Oilfield Company, Panjin 124010, P. R. China*

E-mail address: zcheng21@xsyu.edu.cn (Z. Cheng); rongrong20220120@163.com (M. Xiao); sktong1987@126.com (S. Tong); lh_zhangshuang@petrochina.com.cn (S. Zhang); myxxsyu@163.com (Y. Miao); abc772432442@hotmail.com (M. Xiao).

[*] Corresponding author (ORCID: 0000-0002-7087-565X (Z. Cheng)

Cheng, Z., Xiao, M., Tong, S., et al. Molecular insights into interfacial behavior of crude oil-brine-quartz systems under brine dilution. Capillarity, 2025, 18(1): 14-26.

The link to this file is: https://doi.org/10.46690/capi.2026.01.02

Contents

P1: Interfacial tension validation

Molecular dynamics simulations were carried out using LAMMPS (Plimpton, 1995) to determine the interfacial tension of the water-decane system under ambient pressure (0.1 MPa) at temperatures of 298K and 333K. The simulation domain was constructed as a sandwich structure, in which decane molecules were initially placed in the center of the simulation box and water molecules were distributed symmetrically on both sides along the z-direction, forming two equivalent liquid-liquid interfaces. Periodic boundary conditions were applied in all three directions. Water was represented by the SPC/FW model, while decane was described using the all-atom OPLS-AA force field. Non-bonded interactions were treated with Lennard-Jones potentials and long-range electrostatics computed using the PPPM method. To reproduce the target thermodynamic state, the system was equilibrated within the NPT ensemble, during which the simulation cell length in the z-direction was allowed to fluctuate so as to maintain the desired normal pressure, while the *x-y* dimensions were kept fixed to prevent artificial deformation of the interface.

To ensure that the interfacial structure reached thermodynamic equilibrium, the system was first equilibrated for approximately 30 ns, during which the density profiles, interfacial width, and total energy became stable. Subsequently, a 5-ns production run was carried out, from which the components of the pressure tensor were collected with the pressure tensor recorded once every 1 ns. The interfacial tension was calculated following the Kirkwood mechanical route (Kirkwood and Buff, 1949) by evaluating the anisotropy of the pressure tensor across the slab, where the normal and tangential pressure components were obtained from spatially averaged per-atom virial contributions. The final interfacial tension values were obtained by integrating the pressure difference along the z coordinate over the interfacial region (Eq. (S1)).

$$\gamma = \frac{1}{2}\int_{z_1}^{z_2}\left[P_N(z) - P_T(z)\right]dz \tag{S1}$$

where, P_N denotes the normal stress (i.e., P_{zz}), and P_T represents the tangential stress, which is expressed as $P_T(z) = \frac{1}{2}\left[P_{xx}(z) + P_{yy}(z)\right]$.

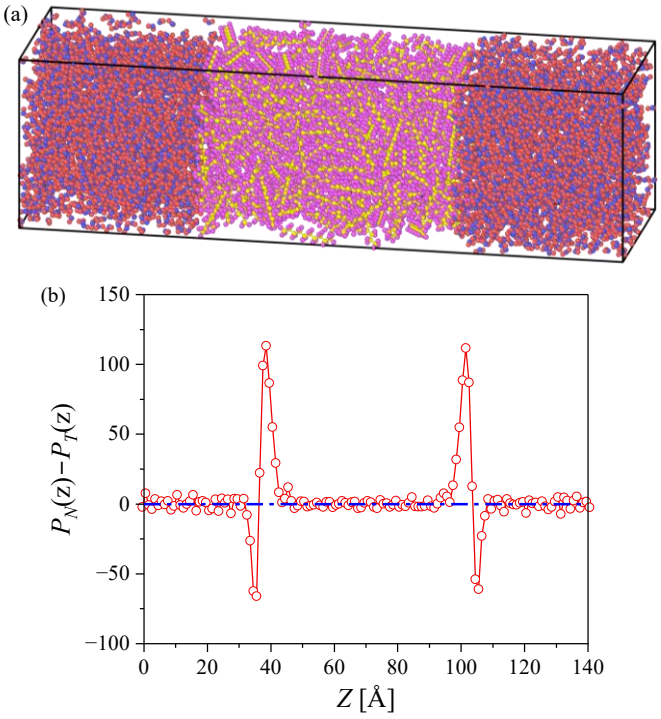

Fig. S1. (a) The model configuration of the simulation of water-decane interfacial tension; (b) an example of the distribution of $P_N(z) - P_T(z)$ along the z-direction under the condition of 333K.

After obtaining the three principal stress components at different sampling times under two temperature conditions, we processed the data using Eq. (S1) to calculate the stress difference along the z-direction, see an example of this procedure shown in Fig. S1b. Subsequently, the stress profiles were integrated to derive the water-decane interfacial tension at 298 and 333 K, followed by averaging, as illustrated in Fig. S2. It can be seen that the values predicted by our molecular simulations agree well with the experimental measurements reported by Goebel and Lunkenheimer (1997) and Zeppieri (2001), thereby confirming the reliability of the force-field parameters and simulation settings used in this study.

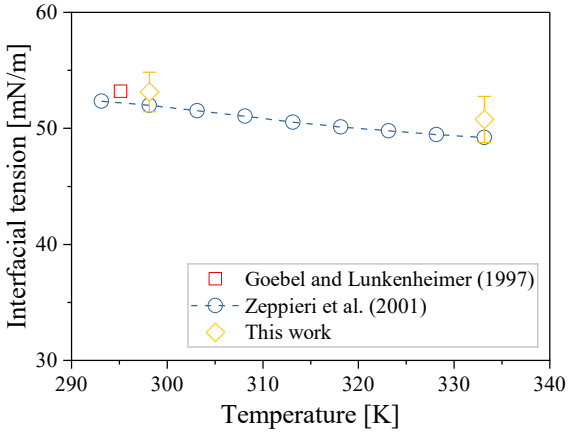

Fig. S2. Comparison of the simulated interfacial tension with previously reported results.

P2: Contact angle validation

P2.1 Water-air-quartz system

All simulations were carried out in LAMMPS (Plimpton, 1995) at a temperature of 300 K. The simulation cell measured 17.4×17.1×1.7 nm^3 in the *x*, *y*, and *z* directions, respectively, and contained a fully hydroxylated α-quartz substrate at the bottom. The force-field parameters for quartz and water were identical to those employed in the main manuscript, ensuring full consistency across all simulations. A spherical water droplet composed of 1121 SPC/FW water molecules was placed directly above the center of quartz surface (Fig. S3a). The remainder of the box above the droplet was left as vacuum to mimic a water-air interface. Periodic boundary conditions were imposed in the x and y directions, while the z direction was fixed (p p f) to prevent unphysical drift of the surface.

Prior to production, the system underwent energy minimization using the conjugate-gradient algorithm, followed by a 0.5-ns strain-release stage in which only the water molecules were allowed to relax, while the bottom quartz layers were held fixed to maintain structural integrity. The system was then equilibrated in the NVT ensemble for 35 ns using a Nosé-Hoover thermostat with a damping constant of 100 fs. A timestep of 1.0 fs was used throughout the simulation. Long-range electrostatics were treated using the PPPM method with an accuracy of 0.0001, and a cutoff of 12 Å was applied to short-range van der Waals interactions. To prevent deformation of the substrate, all quartz atoms were held fixed except for the hydrogen atoms on the upper hydroxylated surface, which were allowed to move freely so as to capture realistic surface relaxation and hydrogen-bond formation at the water-quartz interface.

During the final 5 ns of simulation, the trajectory and water density were recorded for structural and thermodynamic analysis. The equilibrium droplet shape was determined by extracting the molecular density field (Fig. S3c), and fitting the resulting profile to quantify the contact angle (Fig. S3d). This approach ensures a robust and statistically averaged characterization of the wetting state.

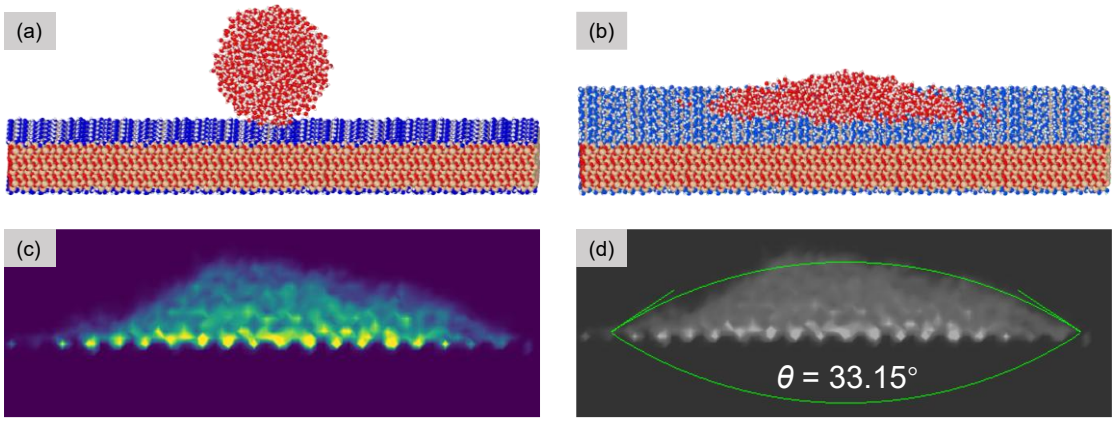

Fig. S3. (a) Initial configuration of the water-quartz system; (b) equilibrium configuration showing the spread water droplet on the quartz surface; (c) water density distribution obtained from the field-based density map, where yellow indicates regions of higher density and darker colors indicate lower density; (d) determination of the contact angle using the MATLAB script described in the manuscript.

Fig. S3 illustrates the evolution of the water droplet from the initial configuration to the final equilibrium state, along with the procedure used to determine the contact angle. The measured contact angle is 33.15°, which is in good agreement with the value reported by Friedman et al. (2013), who measured a water-air-quartz contact angle of approximately 28° under ambient conditions at 300 K. The close correspondence between our simulated value and the experimental measurement demonstrates the reliability of our simulation setup and parameterization.

P2.2 Water-decane-quartz system

To further validate the wetting characteristics of multicomponent systems, molecular dynamics simulations were also conducted for the water-decane-quartz system at 323 K. The simulation domain measured 20.8×34.3×1.7 nm^3 in the x, y, and z directions, respectively, and contained a fully hydroxylated quartz substrate at the bottom. A cylindrical decane phase was initially positioned at the center of the quartz surface, while the remaining space in the simulation cell was filled with water molecules, thereby forming an open system. All force-field parameters for quartz, water, and decane were identical to those used in the main manuscript to ensure methodological consistency. In addition, a 2.6-nm vacuum layer was inserted above the liquid region, and a reflective wall was applied at the top boundary to prevent molecular escape. Periodic boundary conditions were imposed in the x and y directions, whereas a fixed boundary was applied along z. Similar to the water-air-quartz simulations, the system was first subjected to energy minimization followed by a short strain-release stage. It was then equilibrated in the NVT ensemble using a Nosé-Hoover thermostat with a damping constant of 100 fs, and a timestep of 1.0 fs was employed throughout the simulation. Long-range electrostatic interactions were treated using the PPPM algorithm with a target accuracy of 0.0001, and a cutoff of 12 Å was applied for Lennard-Jones interactions. To prevent unphysical deformation of the solid phase, all quartz atoms were held fixed except for the hydrogen atoms on the hydroxylated surface, which were allowed to move freely in order to capture realistic interfacial relaxation and hydrogen-bond dynamics. During the final stage of the simulation, configurations were sampled at regular intervals (1 ns) for characterization of the equilibrium wetting morphology, density distribution, and the contact angle of the water-decane-quartz system.

Fig. S4 presents the distribution of the decane droplet after the system reached equilibrium. The decane density profile was extracted and fitted using a MATLAB script, yielding a contact angle of 24.2°. This result is in excellent agreement with the experimental measurement reported by Duffy et al. (2021), who found that the contact angle of the water-decane-quartz system under ambient conditions at 323.15 K is approximately 24.6°. The close correspondence between our simulated value and the experimental benchmark further confirms the reliability and accuracy of our simulation setup and parameterization.

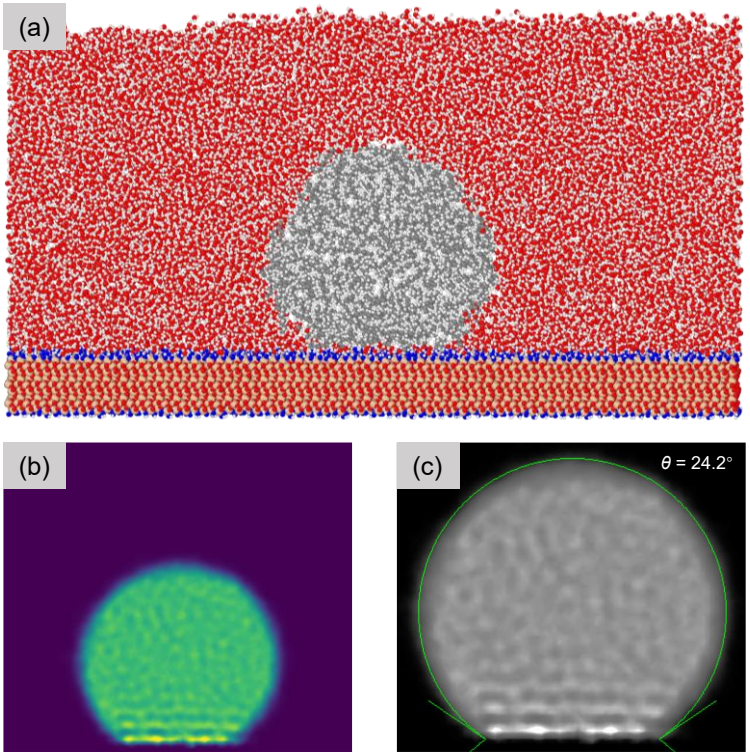

Fig. S4. (a) Distribution of water and decane after the system reached the steady state; (b) decane density profile extracted at equilibrium; (c) determination of the contact angle for the water-decane-quartz system.

P3: Dynamic behavior of hydrogen bonds

In this section, we further analyzed the temporal evolution of hydrogen bonding between quartz surface hydroxyl groups and water molecules under various brine conditions for different crude oil types. The analysis spans both the pre-equilibration period and the subsequent equilibrium (sampling) stage. As shown in Fig. S5, the number of hydrogen bonds exhibits no pronounced fluctuations over time across the different oil systems. Overall, the hydrogen-bond populations remain comparable among the various crude oils and dilution ratios, which is consistent with the trend observed for the average number of hydrogen bonds at equilibrium (see Fig. 12 in the revised manuscript). It is worth noting that a 0.2 ns pre-simulation was performed prior to outputting atomic trajectories to release residual system stresses. In other words, trajectory recording commenced only after 0.2 ns. Throughout the production run, the hydrogen-bond count remained relatively stable, indicating that hydrogen bonds between interfacial water molecules and surface hydroxyl groups form rapidly and are only marginally influenced by the subsequent solution conditions or simulation time.

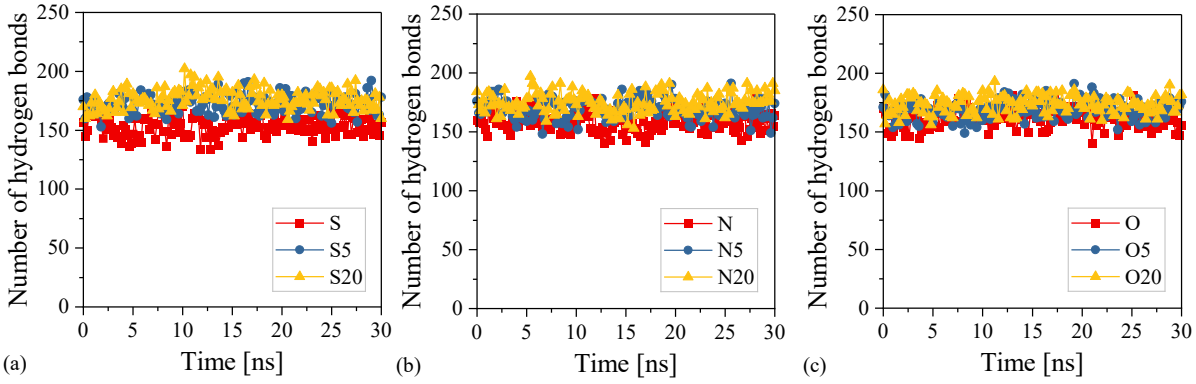

Fig. S5. Variations in the number of hydrogen bonds between −OH and H_2O under brine dilution for (a) S-containing crude oil, (b) N-containing crude oil, and (c) O-containing crude oil, respectively.

P4: Analysis of the lifetime of hydrogen bonds and angle distribution

The identification of hydrogen bonds in this work follows the geometric criteria established by Luzar and Chandler (1996), whereby a hydrogen bond is considered to exist when the distance between the two oxygen atoms is less than 3.5 Å and the O–H···O angle is smaller than 30°.

For any given hydrogen bond, its existence at time t is defined as follows,

$$h(t)=\begin{cases}1, & \textit{if the criteria is met}\\ 0, & \textit{otherwise}\end{cases} \tag{S2}$$

We employed the intermittent autocorrelation function to characterize the lifetime of hydrogen bonds, allowing for transient breaking. That is, if a donor-acceptor pair reforms a hydrogen bond after a brief dissociation, it is still considered the same hydrogen-bonded pair. The function is defined as follows,

$$C(t)=\frac{\langle h(0)h(t)\rangle}{\langle h\rangle} \tag{S3}$$

where $h(0)$ and $h(t)$ represent the fraction of time that a hydrogen bond exists simultaneously at times 0 and t, with $\langle h\rangle$ serving as a normalization factor. Moreover, the characteristic lifetime of the hydrogen bond is defined as follows,

$$\tau_c=\int_0^{\infty}C(t)\,dt \tag{S4}$$

Based on this approach, we obtained the autocorrelation functions of hydrogen bonds between −OH groups and H_2O molecules under different crude oil types and various brine dilution ratios, as shown in Fig. S6.

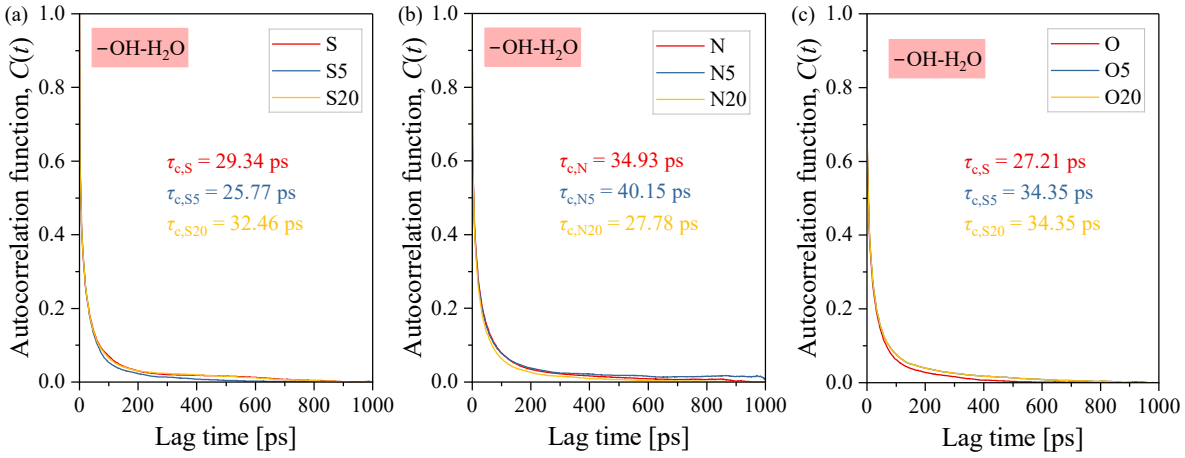

Fig. S6. Autocorrelation function VS lag time under brine dilution for (a) S-containing crude oil, (b) N-containing crude oil, and (c) O-containing crude oil, respectively.

From the decay behavior of the intermittent autocorrelation function $C(t)$ and the number of hydrogen bonds at equilibrium shown in Fig. 12 of the revised manuscript, it is evident that all three systems exhibit a pronounced two-timescale decay in their autocorrelation functions. The rapid decay corresponds to the breaking and reformation of short-lived, localized hydrogen bonds, typically on the order of tens of picoseconds, whereas the long-tail decay reflects the retention of hydrogen bonds near the surface, constrained by geometric or chemical factors, on the order of hundreds of picoseconds.

The statistical average hydrogen-bond counts (Fig. 12) follow the order: S5 > S20 > S, N20 > N5 > N, and O20 > O5 > O. If only the hydrogen-bond numbers are considered, systems such as S5, N20, and O20 appear to be more hydrogen-bond rich. However, the average continuous lifetime calculated from Eq. S4 does not strictly correlate with the hydrogen-bond count. For example, $\tau_{c,S}$ is relatively short, while $\tau_{c,S20}$ is higher; similarly,

$\tau_{c,N5}$ is significantly longer than $\tau_{c,N20}$. This discrepancy can be attributed to the fact that hydrogen-bond count reflects instantaneous occupancy, whereas τ_c measures the dynamic stability of individual bonds. Under certain dilution conditions, the interface may exhibit numerous but short-lived instantaneous hydrogen-bond formations (higher occupancy but more dynamic), whereas in other conditions, fewer hydrogen bonds may form, but they are more linear and energetically favorable, leading to extended lifetimes.

Collectively, these results indicate that solution dilution modulates interfacial molecular coverage, aggregation and dissociation, and solute-water interactions, thereby influencing both the number and dynamics of hydrogen bonds. This explains the apparently inconsistent but physically coherent observations.

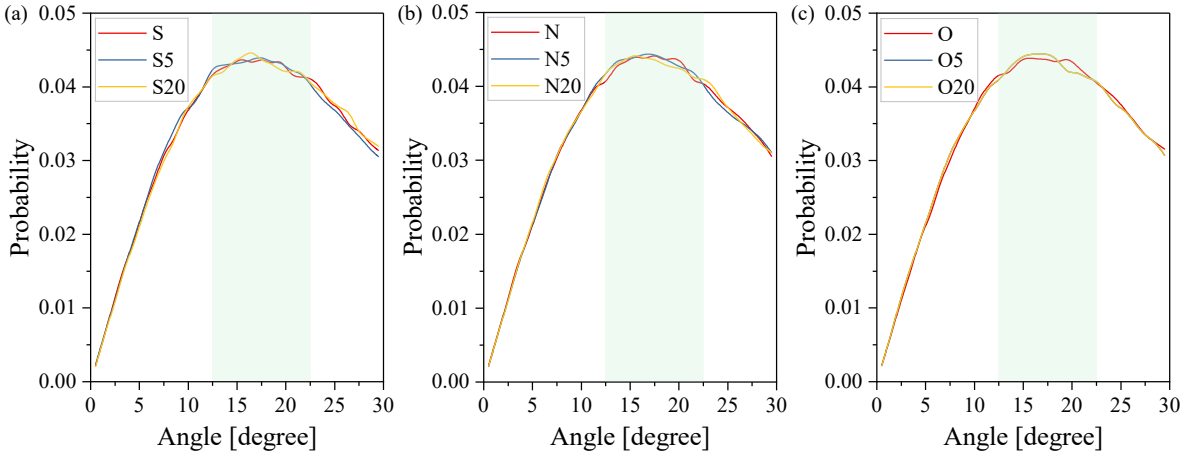

Fig. S7. Probability distribution of hydrogen-bond angle at equilibrium under various brine dilution conditions for (a) S-containing crude oil, (b) N-containing crude oil, and (c) O-containing crude oil, respectively.

Furthermore, we analyzed the probability distributions of hydrogen-bond angles and distances under different conditions (Figs. S7 and S8). The hydrogen-bond angles are predominantly distributed in the range of 12.5°-22.5°, while the distances mainly fall within 2.6-2.8 Å. Across different crude oil types, brine dilution has a negligible effect on the overall distributions of angles and distances. However, variations in dilution ratios lead to subtle changes in the distribution features, which further support the observations in Fig. S6. Specifically, more concentrated angle and distance distributions correspond to longer-lived hydrogen bonds, consistent with the autocorrelation analysis.

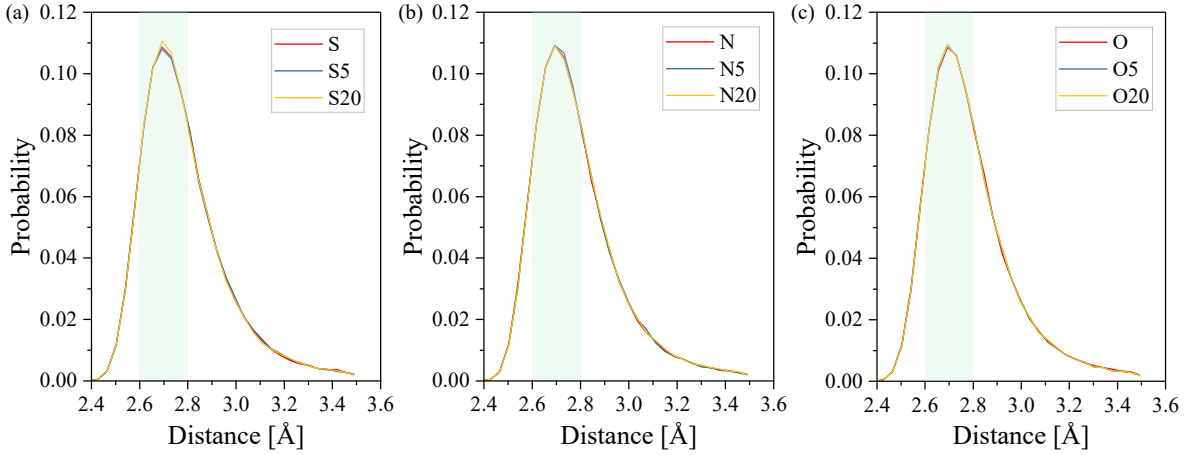

Fig. S8. Probability distributions of O–O distances at equilibrium under various brine dilution conditions for (a) S-containing crude oil, (b) N-containing crude oil, and (c) O-containing crude oil, respectively.

References

Duffy, T.S., et al., Capillary contact angle for the quartz-distilled water-normal decane interface at temperatures up to 200 °C. Colloids and Surfaces A: Physicochemical and Engineering Aspects, 2021. 609: 125608.

Friedman, S.R., M. Khalil, and P. Taborek, Wetting transition in water. Physical review letters, 2013. 111(22): 226101.

Goebel, A. and K. Lunkenheimer, Interfacial tension of the water/n-alkane interface. Langmuir, 1997. 13(2): 369-372.

Kirkwood, J.G. and F.P. Buff, The statistical mechanical theory of surface tension. The Journal of Chemical Physics, 1949. 17(3): 338-343.

Luzar, A., Effect of Environment on Hydrogen Bond Dynamics in Liquid Water. Physical Review Letters, 1996. 76(6): 928-931.

Plimpton, S. Fast parallel algorithms for short-range molecular dynamics. Journal of Computational Physics, 1995. 117(1): 1-19.

Zeppieri, S., J. Rodríguez, A. López de Ramos, Interfacial tension of alkane+ water systems. Journal of Chemical & Engineering Data, 2001. 46(5): 1086-1088.